

Flexible $Ti_3C_2T_x$ /Graphene Films with Large-Sized Flakes for Supercapacitors

Tiezhu Guo, Maosen Fu, Di Zhou,* Lixia Pang, Jinzhan Su, Huixing Lin, Xiaogang Yao, and Antonio Sergio Bezerra Sombra

The new 2D $Ti_3C_2T_x$ MXene material is widely studied in the field of supercapacitors. However, the electrochemical performance is discounted due to $Ti_3C_2T_x$ film's compact self-stacking phenomenon. Therefore, the synthesized flexible self-supporting $Ti_3C_2T_x$ /graphene composite membrane effectively alleviates this inherent disadvantage. Unlike using the traditional reduction graphene oxide, the structural integrity and large-sized flakes of graphene are synthesized through anhydrous ferric chloride ($FeCl_3$)-intercalated natural graphite flakes; the obtained composite membrane with high electron transfer capability due to graphene and $Ti_3C_2T_x$ nanosheets shows fewer defects and faster electrolyte ion transport kinetics due to high porosity and specific surface area. The assembled self-supporting binder-free symmetric supercapacitor shows an ultrahigh gravimetric energy density of 13.1 Wh kg^{-1} at a power density of 75 W kg^{-1} . Herein, a new perspective for the mechanism analysis of inhibiting self-stacking of MXene is provided.

energy-storage fields, such as supercapacitors and $Li^+/Na^+/K^+$ batteries, due to its outstanding electrical conductivity, surface hydrophilicity, and electrochemical properties.^[3–5] So far, the most common strategy for preparing $Ti_3C_2T_x$ is to etch MAX in hydrofluoric acid (HF), HF-containing, or HF-forming etchants by wet etching, with functional groups such as $-O$, $-F$, and $-OH$ on the surface, represented by T_x in the general formula $M_{n+1}X_nT_x$.^[6,7]

As previously reported, HF is a highly corrosive acid that penetrates skin, muscle tissue, and bone. Due to its risk, the most widely used alternative to HF is to use a mixture of hydrochloric acid and fluoride salts to form in situ HF. In the current in situ HF etching methods, different etching environments and process parameters

will affect the product performance and the best application fields, such as, the synthetic multilayer $Ti_3C_2T_x$ that was etched using in situ HF by adding lithium fluoride (LiF, LiF: Ti_3AlC_2 molar ratio of 5) into hydrochloric acid (6 M HCl) and was ultrasonic stripped into delaminated $Ti_3C_2T_x$ nanosheets, the strategy also known as $Ti_3C_2T_x$ “clay” method.^[8] The sonication step can lead to the reduction of $Ti_3C_2T_x$ nanosheet sizes and the generation of defects, and higher power and longer time will show more defects and smaller sizes.^[6] Interestingly, these

1. Introduction

MXenes, as emerging 2D transition metal carbides, nitrides, and carbonitrides with a general formula of $M_{n+1}X_n$, are prepared by selective etching of element A in ternary cermet MAX phase. M is an early-transition metal or metal solid solution (Ti, V, Nb, Mo, Hf, Zn, Sc, etc). A represents the element Al or Si, X is carbon (C) and/or nitrogen (N), and $n = 1, 2, \text{ or } 3$.^[1,2] As the first MXene studied, $Ti_3C_2T_x$ has been widely studied and explored in the

T. Guo, Prof. D. Zhou
Key Laboratory of Multifunctional Materials and Structures
Ministry of Education, & International Center for Dielectric Research
School of Electronic Science and Engineering
Xi'an Jiaotong University
Xi'an 710049, Shaanxi, China
E-mail: zhoudi1220@xjtu.edu.cn, zhoudi1220@gmail.com


Dr. M. Fu
Shaanxi Materials Analysis and Research Center
School of Materials Science and Engineering
Northwestern Polytechnical University
Xi'an, Shaanxi 710072, China

Prof. L. Pang
Micro-optoelectronic Systems Laboratories
Xi'an Technological University
Xi'an 710032, Shaanxi, China

Prof. J. Su
International Research Centre for Renewable Energy
State Key Laboratory of Multiphase Flow in Power Engineering
Xi'an Jiaotong University
Xi'an 710049, China

Prof. H. Lin, Dr. X. Yao
Key Laboratory of Inorganic Functional Material and Device
Shanghai Institute of Ceramics
Chinese Academy of Sciences
Shanghai 200050, China

Dr. A. S. B. Sombra
Telecommunication and Materials Science and Engineering of Laboratory (LOCEM)
Physics Department
Federal University of Ceará (UFC)
Pici Campus, Fortaleza, Ceará 60455-760, Brazil

 The ORCID identification number(s) for the author(s) of this article can be found under <https://doi.org/10.1002/sstr.202100015>.

DOI: 10.1002/sstr.202100015

smaller and more defective nanosheets are popular in catalysis and biomedical applications.^[9,10] On the contrary, when applied to electrode materials of the supercapacitor field, large-sized flakes are more conducive to achieving excellent electrochemical performance due to their high conductivity, superior mechanical strength, and the realization of self-supporting film electrode without any binder or conductive agent. Therefore, it is necessary for us to pay attention to and select suitable $\text{Ti}_3\text{C}_2\text{T}_x$ preparation methods for different application fields. Minimally intensive layer delamination (MILD, by optimizing the concentration of LiF/HCl , it is different from the “clay” LiF/HCl method) method has been the choice for studies/applications, where larger-sized flakes and small defects are favorable, which were only processed by manual shaking without sonication treatment.^[11–15] Consequently, the preparation of high-quality $\text{Ti}_3\text{C}_2\text{T}_x$ by the MILD method is promising in the field of supercapacitors.

To give full play to $\text{Ti}_3\text{C}_2\text{T}_x$'s excellent inherent performances, one of the most critical problems to be solved for $\text{Ti}_3\text{C}_2\text{T}_x$ as electrodes materials of supercapacitors is how to reduce the self-restacking and aggregation between nanosheets. Because of the robust Van der Waals interaction in the drying and synthesis processes,^[16] the self-restacking phenomenon has been proved to significantly reduce ion mobility, which is not conducive to fast charge–discharge of devices under high current density. To improve the problem, various materials such as nano-Ag particles,^[17] conductive polymer PEDOT: PSS,^[18] carbon nanotubes (CNTs),^[19] and reduced graphene oxide (RGO)^[20–22] were introduced into $\text{Ti}_3\text{C}_2\text{T}_x$ to prepare composite self-supporting films by vacuum filtration. $\text{Ti}_3\text{C}_2\text{T}_x$ -RGO hybrid materials have been reported in some literatures. For example, Yan et al. prepared RGO with a positive surface charge modified by poly(diallyldimethylammonium chloride) (PDDA); electrostatic self-assembly can significantly prevent $\text{Ti}_3\text{C}_2\text{T}_x$ from stacking and effectively improve the performance of $\text{Ti}_3\text{C}_2\text{T}_x$ hybrid film as an electrode material for supercapacitors.^[23] Shen et al. have prepared RGO/ $\text{Ti}_3\text{C}_2\text{T}_x$ nanopowder for use in Li^+ batteries.^[24] It also shows better electrochemical performance than pure $\text{Ti}_3\text{C}_2\text{T}_x$. Although the $\text{Ti}_3\text{C}_2\text{T}_x$ -RGO composite film has achieved a certain effect to improve the self-stacking phenomena,^[25–27] however, graphene oxide (GO) was used as the precursor of graphene, with a conductivity of only about $5 \times 10^{-6} \text{ S cm}^{-1}$ due to a large amount of oxygen-containing functional groups on its surface and edge.^[28] Therefore, it is necessary to fully realize the reduction of GO. Because the reduction degree of RGO is highly dependent on the synthesis process, reducing agent, or the later heat-treatment process, the flake sizes, oxygen content, and defect levels of RGO have a strong impact on the properties of graphene. Therefore, it is of certain significance to design and develop $\text{Ti}_3\text{C}_2\text{T}_x$ -graphene-based electrode materials with higher electrochemical performance. To address this problem, we prepared graphene with good structural integrity by anhydrous ferric chloride (FeCl_3) intercalation into natural graphite flakes and then obtained by sodium borohydride (NaBH_4) aqueous solution expansion, without oxidation by strong oxidants.

In this work, we demonstrate the fabrication of $\text{Ti}_3\text{C}_2\text{T}_x$ /graphene composite films through $\text{Ti}_3\text{C}_2\text{T}_x$ and graphene nanosheets with large-sized flakes and good structural integrity self-assembly to obtain supercapacitors with outstanding rate

capability and cyclic stability. The results of this study mainly indicate that the introduction of graphene into $\text{Ti}_3\text{C}_2\text{T}_x$ improves the specific capacitance, mainly due to the improvement in specific surface area rather than the interlayer spacing. Specifically, graphene is freely distributed in $\text{Ti}_3\text{C}_2\text{T}_x$, different from conclusions in some literatures that the specific capacitance of the material is optimized by increasing the $\text{Ti}_3\text{C}_2\text{T}_x$ interlayer spacing. It provides new insights for $\text{Ti}_3\text{C}_2\text{T}_x$ /graphene electrode materials with excellent electrochemical properties.

2. Results and Discussion

2.1. Synthesis and Characterization of Graphene and MXene

Graphene nanosheets were prepared by FeCl_3 -intercalated natural graphite flakes using the molten salt method and then obtained by sodium borohydride (NaBH_4) aqueous solution expansion. Scanning electron microscopy (SEM) of graphene is shown in **Figure 1a**. To reduce surface energy, graphene nanosheets form spontaneous curls and wrinkles, and their particle sizes distribution D_{50} is about $11.7 \mu\text{m}$ (Figure S1a, Supporting Information, D_{50} means that the volume with particle sizes less than $11.7 \mu\text{m}$ accounts for 50% of the total volume). Transmission electron microscopy (TEM) image clearly shows large areas of ultrathin graphene with high transparency and slightly crimped folds at the edges (Figure 1b and Figure S2, Supporting Information). The inserted selected-area electron diffraction (SAED) pattern also exhibits the lattice symmetry of the nanosheets, as well as high crystallinity of the graphene nanosheets. In the structural studies of graphene, I_D/I_G is commonly used in Raman spectroscopy to represent the degree of structural defects. Figure 1c shows the intensity ratio of I_D/I_G , which is only 0.23, which indicates that graphene has small defects, which is much smaller than that of RGO.^[29] The XRD pattern shows the multilayered inplane structure of graphene with the interlayer spacing of 0.34 nm, according to the strong peak (002) in the center at $2\theta = 26.7$ (Figure S3, Supporting Information).

$\text{Ti}_3\text{C}_2\text{T}_x$ self-supported film electrode is used to prepare supercapacitors. MILD method-etched MAX phase has the advantages of high conductivity, stable environment, excellent mechanical properties, large-sized flakes, etc. Ti_3AlC_2 powder was etched at 35°C ($12 \text{ M LiF}/9 \text{ M HCl}$) for 24 h, and the mixture was washed separately in 1 M HCl , 1 M LiCl , and deionized water under centrifugation (5 min per cycle at 3500 rpm) to pH of ≈ 6 . Two important phenomena were observed here, dark-green $\text{Ti}_3\text{C}_2\text{T}_x$ supernatant appeared on the upper layer of the centrifuge tube, indicating that peeling occurred during repeated washing, and centrifugation without any other mechanical vibration. At the bottom of the centrifuge tube, a significant volume swelling phenomenon was observed compared with that before the first washing, and two layers of different colors of the swelling sediment, $\text{Ti}_3\text{C}_2\text{T}_x$ slurry (black) and nonetched $\text{Ti}_3\text{AlC}_2/\text{Ti}_3\text{C}_2\text{T}_x$ mixture (grayish), were clearly observed (Figure S4, Supporting Information). X-ray diffraction (XRD) measurements were carried out for $\text{Ti}_3\text{C}_2\text{T}_x$ slurry and $\text{Ti}_3\text{C}_2\text{T}_x$ supernatant, and the two patterns are very similar (Figure 1d). The large-sized-flake $\text{Ti}_3\text{C}_2\text{T}_x$ nanosheets could be clearly observed through SEM images (Figure 1e). It was further proved by the TEM image that

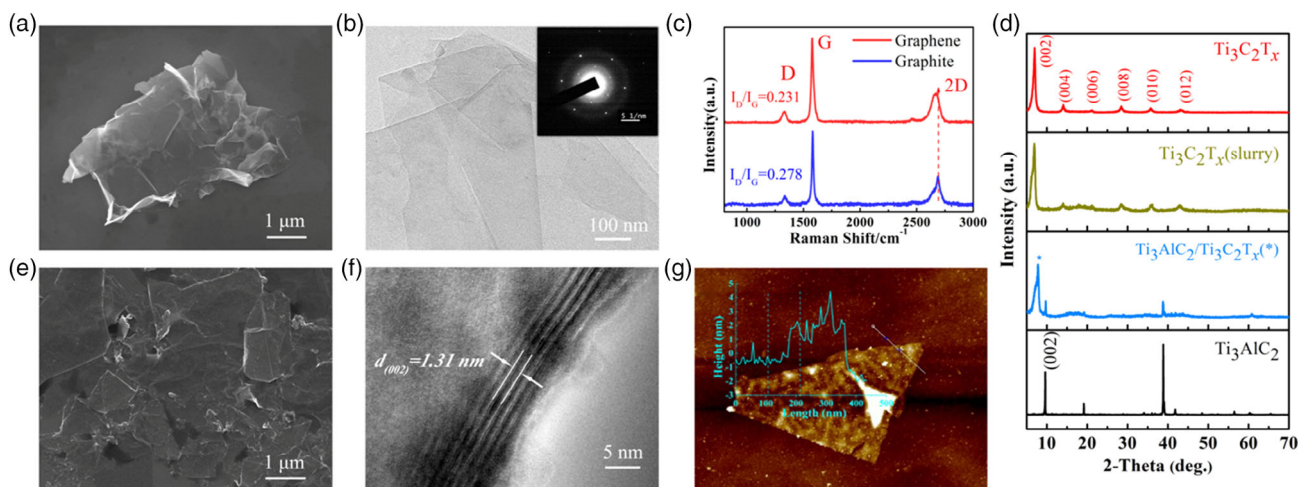


Figure 1. a) Top-view SEM image of graphene. b) TEM image of few layers of exfoliated graphene (the inset shows the SAED pattern). c) Raman patterns of graphene. d) XRD patterns of delaminated $\text{Ti}_3\text{C}_2\text{T}_x$ supernatant, $\text{Ti}_3\text{C}_2\text{T}_x$ slurry, and dried powder of $\text{Ti}_3\text{AlC}_2/\text{Ti}_3\text{C}_2\text{T}_x$ mixture. e) Top-view SEM image of $\text{Ti}_3\text{C}_2\text{T}_x$. f) TEM image of few layers of $\text{Ti}_3\text{C}_2\text{T}_x$. g) AFM image of the delaminated $\text{Ti}_3\text{C}_2\text{T}_x$ nanosheets.

about five layers of $\text{Ti}_3\text{C}_2\text{T}_x$ can be observed from the edge of the delaminated $\text{Ti}_3\text{C}_2\text{T}_x$ nanosheets (Figure 1f) and the large lateral size of several micrometers (Figure S5, Supporting Information). The atomic force microscopy (AFM) image shown in Figure 1g shows that most of the delaminated $\text{Ti}_3\text{C}_2\text{T}_x$ nanosheets are about 2 nm thick. Therefore, these large-sized flakes and smaller-defect nanosheets have tremendous potential to be readily assembled into flexible films. The particle size distribution was further analyzed by a laser particle size analyzer (Figure S1b, Supporting Information). These flakes' sizes of $\text{Ti}_3\text{C}_2\text{T}_x$ were about $4.88 \mu\text{m}$ (D_{50}), which were similar to the results reported in the literature.^[6] To better understand the surface properties of graphene and $\text{Ti}_3\text{C}_2\text{T}_x$, the zeta potentials of graphene, $\text{Ti}_3\text{C}_2\text{T}_x$, and the mixed solution were measured to be -8.8 , -31.4 , and -59.8 mV (Figure S6, Supporting Information), respectively. Due to electrostatic repulsion, the two solutions could be uniformly dispersed without apparent agglomeration, which avoids the occurrence of film brittleness.

2.2. Characterization of MXene/Graphene Film

SEM was used to observe the microstructure and morphology of $\text{Ti}_3\text{C}_2\text{T}_x/\text{graphene}$ (denoted as M/G- x , where x is the mass percent of graphene to $\text{Ti}_3\text{C}_2\text{T}_x$, such as M/G-5, M/G-10, and M/G-15) and $\text{Ti}_3\text{C}_2\text{T}_x$ films.

Figure 2a clearly shows obvious wrinkles on the surface of pure $\text{Ti}_3\text{C}_2\text{T}_x$ membrane, and the surface of M/G-10 composite film appeared obviously on 2D nanosheets in addition to wrinkles, as seen from top-view SEM images (Figure 2b). Similarly, there are many 2D nanosheets upturned on the M/G-5 and M/G-15 films' surface (Figure S7, Supporting Information). The layered structure of $\text{Ti}_3\text{C}_2\text{T}_x$ film can be clearly observed from the cross-sectional SEM image (Figure 2c). After introducing graphene into $\text{Ti}_3\text{C}_2\text{T}_x$, it can be clearly observed that the flexible wrinkled graphene is freely distributed in $\text{Ti}_3\text{C}_2\text{T}_x$ nanosheets (Figure 2d), which was further approved by the

inhomogeneous distribution of Ti and C elements throughout the whole composite (Figure 2e,f). Further analysis of the change of M/G-10 composite film interlayer spacing has essential significance for understanding the electrochemical storage mechanism. Pure $\text{Ti}_3\text{C}_2\text{T}_x$ exhibits the strong diffraction peak (002) at 6.74° , and the corresponding interlayer spacing of 1.31 nm, which is typical for $\text{Ti}_3\text{C}_2\text{T}_x$ with water between the layers.^[30] The diffraction peak (002) of M/G-10 composite film shifts to 6.48° , and the responsive interlayer spacing is 1.36 nm (Figure 2i). The complete XRD patterns from 5° to 45° are shown in Figure S8, Supporting Information. Unlike the reported literatures,^[21,23] there was no noticeable movement toward a small angle. Combined with SEM cross-sectional analysis, we believe that flexible wrinkled graphene can reduce the self-stacking of $\text{Ti}_3\text{C}_2\text{T}_x$ at a macrolevel (relative layer-by-layer self-assembly: 1–2 nm scale), which is mainly due to its free dispersion in the interlayer of $\text{Ti}_3\text{C}_2\text{T}_x$, rather than the microscopic layer-by-layer self-assembly. One reason for this may be that large-sized graphene is prone to in-plane warping and wrinkling, which is not conducive to forming layer-by-layer self-assembly. Another important reason may be that there are fewer large nanosheets than small nanosheets with the same mass of graphene. Furthermore, N_2 adsorption/desorption (BET) were tested to verify the mitigative self-stacking in M/G-10, which in specific surface area of the M/G-10 film ($193.9 \text{ m}^2 \text{ g}^{-1}$) is much larger than pure $\text{Ti}_3\text{C}_2\text{T}_x$ ($0.13 \text{ m}^2 \text{ g}^{-1}$) (Figure S9, Supporting Information). Whatever role graphene plays, N_2 adsorption/desorption test results show that $\text{Ti}_3\text{C}_2\text{T}_x/\text{graphene}$ has a larger specific surface area than pure $\text{Ti}_3\text{C}_2\text{T}_x$.^[22,23] Table S1, Supporting Information, shows that pure $\text{Ti}_3\text{C}_2\text{T}_x$ has a high conductivity, which decreases slightly after introduction of graphene, but it is also significantly higher than $\text{Ti}_3\text{C}_2\text{T}_x/\text{RGO}$ as reported in the literatures.^[21–23] Figure 2g shows that pure $\text{Ti}_3\text{C}_2\text{T}_x$ film surfaces exhibit a hydrophilic contact angle of about 35° , consistent with the literature.^[3] After 15 s of contact between the droplets with the $\text{Ti}_3\text{C}_2\text{T}_x$ film, the contact angle quickly decreases to 23° , and the film surface is almost

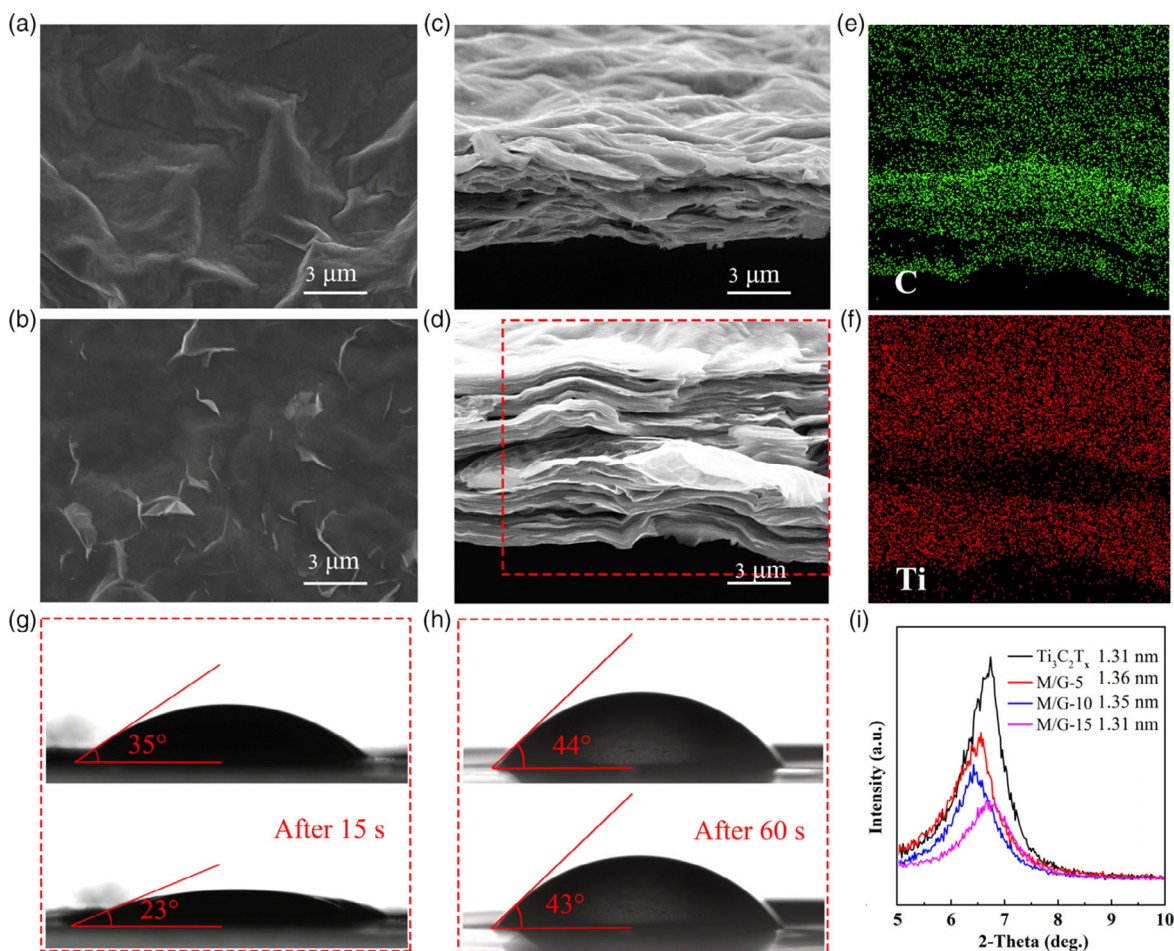


Figure 2. Top-view SEM images of a) $\text{Ti}_3\text{C}_2\text{T}_x$ and b) M/G-10. Cross-sectional SEM images of c) $\text{Ti}_3\text{C}_2\text{T}_x$ and d) M/G-10. e, f) The corresponding energy-dispersive X-ray (EDS) mapping images of the M/G-10 (the area marked in red in image d). Water contact angles of g) $\text{Ti}_3\text{C}_2\text{T}_x$ and h) M/G-10 film. i) XRD patterns of the $\text{Ti}_3\text{C}_2\text{T}_x$ film and $\text{Ti}_3\text{C}_2\text{T}_x$ /graphene films at low Bragg angles.

completely wet, indicating that the pure $\text{Ti}_3\text{C}_2\text{T}_x$ film has poor water resistance. This is one of the reasons why $\text{Ti}_3\text{C}_2\text{T}_x$ film can be easily redispersed in aqueous solutions. The hydrophilic contact angle of the M/G-10 composite film is about 44°. The slight increase in the contact angle of the composite film is mainly due to the hydrophobicity of graphene, which is attributed to the absence of strong oxidation during the process of flake graphite peeling into graphene, with only a small number of oxygen-containing functional groups on the surface or edge. However, after the contact time reaches 60 s, the contact angle only drops slightly (Figure 2h), indicating that the water-resistance stability of the composite film is significantly improved, which can be utilized to improve the service life and experiment operation of the film.

To further analyze the surface electron states and interactions of M/G-10 and $\text{Ti}_3\text{C}_2\text{T}_x$ films, X-ray photoelectron spectroscopy (XPS) tests were conducted. The presence of Ti, C, O, F, and Cl elements was confirmed in Figure 3a. The high-resolution Ti $2p_{3/2}$ was subdivided into three environments located at 455.8, 457.2, and 458.8 eV, which responded to the Ti–C, Ti (II), and Ti–O bonds, respectively (Figure 3b).^[23] It can be determined that

Ti–O bond peak enhancement in M/G-10 film is mainly due to the interaction between $\text{Ti}_3\text{C}_2\text{T}_x$ and a small number of functional groups on the surface or edge of graphene, in which the O/Ti ratios of M/G-10 and $\text{Ti}_3\text{C}_2\text{T}_x$ are 0.80 and 0.71, respectively (XPS results are shown in Table S2, Supporting Information). It indicates the chemical bonding between $\text{Ti}_3\text{C}_2\text{T}_x$ and graphene nanosheets in the hybrid film. The C 1s core level can be fit into five curves representing the presence of the C–Ti (281.9 eV), C–Ti–O (282.9 eV), C–C (284.8 eV), C–O (285.8 eV), and O–C=O (288.8 eV) bonds, respectively (Figure 3c).^[23,31]

2.3. Electrochemical Performance Evaluation

The electrochemical performance of $\text{Ti}_3\text{C}_2\text{T}_x$ /graphene composite films was assessed using a three-electrode Teflon swagelok configuration in 3 M H_2SO_4 aqueous electrolyte. The H_2SO_4 electrolyte was selected because of its high ionic conductivity, small hydronium ion (H_3O^+) radius, and the ability to provide pseudocapacitance through the occurrence of redox reactions.^[32]

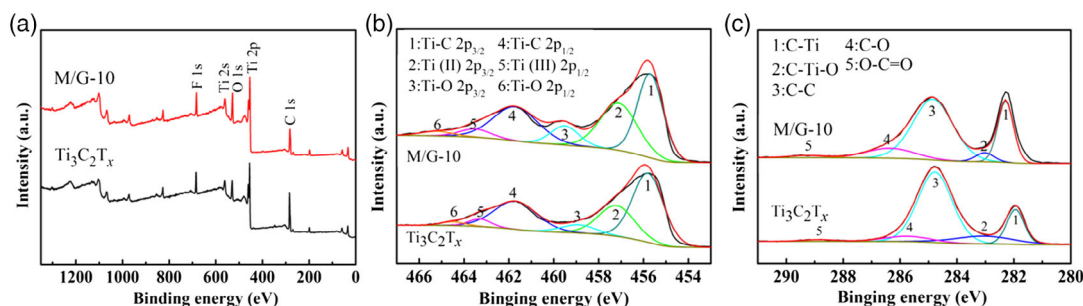
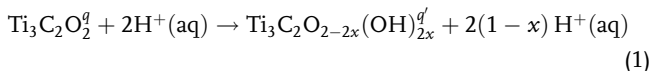


Figure 3. a) XPS survey spectrum of $\text{Ti}_3\text{C}_2\text{T}_x$ and M/G-10 film. b) High-resolution Ti 2p region for $\text{Ti}_3\text{C}_2\text{T}_x$ and M/G-10 film. c) High-resolution C 1s region for $\text{Ti}_3\text{C}_2\text{T}_x$ and M/G-10 film.

The cyclic voltammetry profiles of $\text{Ti}_3\text{C}_2\text{T}_x$ show different capacitive potential windows in other literatures, even under the same test conditions. **Figure 4a** shows no significant redox peaks and resemble those of carbon-based double-layer capacitors, as previously reported.^[8] However, the electrochemical storage mechanism of $\text{Ti}_3\text{C}_2\text{T}_x$ in H_2SO_4 aqueous solution has been demonstrated to be predominantly pseudocapacitance and non-diffusion limited. It is accompanied by the change of reversible interpolation/unplugging of protons along with the change of Ti oxidation state.^[33–35] This charge storage mechanism is based on the Equation (1).^[36]



where x is the surface hydrogen coverage (ranging from 0 to 1) and q is the net charge on the electrode. The integral area of the M/G-10 is slightly larger than that of pure $\text{Ti}_3\text{C}_2\text{T}_x$, indicating a higher

gravimetric specific capacitance. In addition, when the scanning rate increased to 200 mV s^{-1} , the cyclic voltammetry (CV) curves of the hybrid electrode showed no significant distortion (**Figure 4b**), indicating outstanding dynamics at high current densities. M/G-5 and M/G-15 have similar results, as shown in **Figure S10b,c**, Supporting Information. In comparison, the maximum anodic current position of pure $\text{Ti}_3\text{C}_2\text{T}_x$ shows obvious deviation (**Figure S10a**, Supporting Information). **Figure 4c** shows the galvanostatic charge–discharge (GCD) curves, which can be observed to be a deformed triangular shape, but do not appear similar to the redox reaction platform, which is consistent with the CV curves showing no obvious symmetrical peaks of redox. The GCD curves of pure $\text{Ti}_3\text{C}_2\text{T}_x$, M/G-5, and M/G-15 are shown in **Figure S10d–f**, Supporting Information. The gravimetric specific capacitance and areal specific capacitance of M/G-10 were calculated by the CV curves, as shown in **Figure 4d,e**, Supporting Information. The results revealed that M/G-10 has a higher gravimetric specific capacitance of 269.2 F g^{-1} (485.7 mF cm^{-2}) than

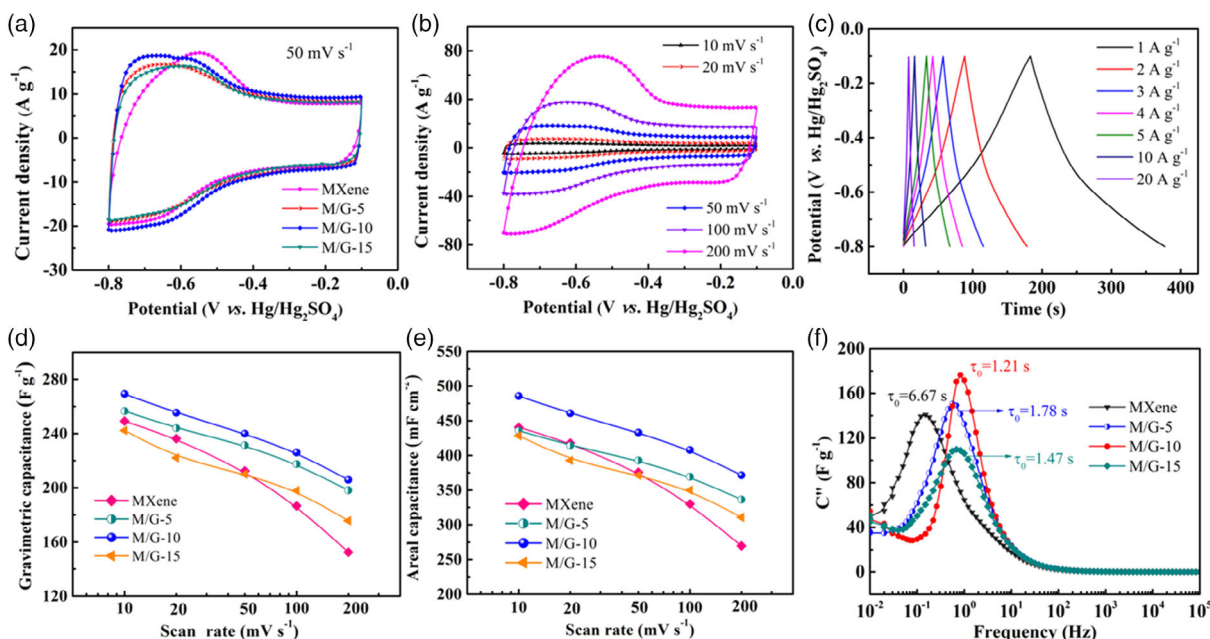


Figure 4. a) CV curves of $\text{Ti}_3\text{C}_2\text{T}_x$ and MXene/graphene films at a scan rate of 50 mV s^{-1} in $3 \text{ M H}_2\text{SO}_4$ electrolyte. b) CV curves of the M/G-10 electrode at different scan rates. c) Galvanostatic charge–discharge curves of M/G-10 at different current densities. d) Gravimetric and e) areal capacitances of $\text{Ti}_3\text{C}_2\text{T}_x$ and MXene/graphene films at different scan rates. f) The relationship between C'' (the imaginary part of the complex capacitance) and frequency.

pure $\text{Ti}_3\text{C}_2\text{T}_x$ of 249.2 F g^{-1} (440.7 mF cm^{-2}) at a scan rate of 10 mV s^{-1} . It is worth noting that M/G-10 has a high rate performance (77%) compared with pure $\text{Ti}_3\text{C}_2\text{T}_x$ (61%) ranging from 10 to 200 mV s^{-1} . This phenomenon is attributed to the spatial stacking gaps caused by physical stacking and entanglement of the large-sized flakes, resulting in greater specific surface area and more exposure of active sites, increasing the ion accessible surface area and promoting electrolyte penetration.

To further demonstrate the rate capability of electrodes and the transport property of ion diffusion, the relationship between capacitance (C) and frequency (F) was studied by electrochemical impedance spectroscopy (EIS). The relationship between C'' (the imaginary part of the complex capacitance) and frequency is shown in Figure 4f. The maximum value of C'' corresponds to the characteristic frequency f_0 ($f_0 = 1/\tau_0$). The relaxation time constant (τ_0) is defined as the minimum time required for the device to release all the energy with an efficiency of more than 50%. The M/G-10 electrode shows minimum relaxation time constant τ_0 of 1.21, which is much smaller than pure $\text{Ti}_3\text{C}_2\text{T}_x$ (6.67 s). The smaller the relaxation time constant, the better the rate performance.

To further study the kinetic and electrochemical energy-storage mechanism of M/G-10 electrode, the current contributed by surface capacitance (i_s) and intercalation–pseudocapacitance current (i_d) was distinguished from the total current (i). According to Equation (2) and (3)^[37]

$$i = i_s + i_d \quad (2)$$

$$i = av^b \quad (3)$$

where a and b are adjustable parameters. The intercalation–pseudocapacitance response current will be proportional to the square root of the scanning rate ($i \sim v^{1/2}$), whereas surface capacitance will show linear current response dependency on the scan rate ($i \sim v$). For $\text{Ti}_3\text{C}_2\text{T}_x$ 2D materials, the capacitance can be distinguished into the diffusion-limited intercalation–pseudocapacitance and nondiffusion-limited surface capacitive capacitance (including pseudocapacitance generated by the change in the valence of Ti ions and double-layer capacitance).^[38]

Figure 5a shows the b -values obtained by $\log i - \log v$ fitting under different voltages of M/G-10 electrode and the range from 0.9 to 1, indicating that the charge-storage process is mainly due

to the contribution of surface capacitance, which is consistent with the high rate performance mentioned earlier. Further quantitative analysis of the proportion of the surface capacitance and intercalation–pseudocapacitance was conducted according to Dunn's method.^[39] The calculations are as follows (Equation (4) and (5)).

$$i(V) = k_1v + k_2v^{1/2} \quad (4)$$

$$\frac{i(V)}{v^{1/2}} = k_1v^{1/2} + k_2 \quad (5)$$

where k_1v and $k_2v^{1/2}$ correspond to the current contributions from the surface capacitance and intercalation–pseudocapacitance, respectively. Figure 5b shows that surface capacitance (shadow area) of the M/G-10 electrode accounts for 72.7% (195.7 F g^{-1}) of the total capacitance at a scan rate of 10 mV s^{-1} . In addition, with the increase in scan rates to 50 and 100 mV s^{-1} , the surface capacitance proportion gradually increases to 81.3% and 86.2% (Figure S11a, b, Supporting Information), respectively. It was not conducive to proton intercalation/deintercalation, which was also one of the reasons for the slight decrease in the capacitance with the increase in scan rates. As shown in Figure 5c, it should be noted that the surface capacitance of M/G-10 electrode was significantly higher (72.7%) than that of pure $\text{Ti}_3\text{C}_2\text{T}_x$ (45.5%, Figure S11c, Supporting Information), which was different from the reported study.^[21] We hypothesized that the main reason for this phenomenon is that the addition of graphene increases the material's macroscopic specific surface area, promotes exposure to more active sites, and increases the ion-accessible surface area. Similarly, it is speculated that one of the reasons for the phenomenon of pure $\text{Ti}_3\text{C}_2\text{T}_x$ having less surface capacitance may be that large-sized flakes have smaller specific surface area and fewer edge active sites than smaller $\text{Ti}_3\text{C}_2\text{T}_x$ flakes.

Factors such as conductivity, hydrophilicity, interlayer spacing, and specific surface area should be considered to analyze the reasons for the optimization of the specific capacitance of M/G-10. It can be inferred from the XRD patterns that the interlayer spacing is not the dominant factor due to the similar interlayer spacing. In addition, as M/G-10 is slightly lower than the conductivity of pure MXene samples, the conductivity can also be excluded. Although the contact angle of the hybrid film is slightly higher than pure $\text{Ti}_3\text{C}_2\text{T}_x$, it is still a hydrophilic film, so it is not

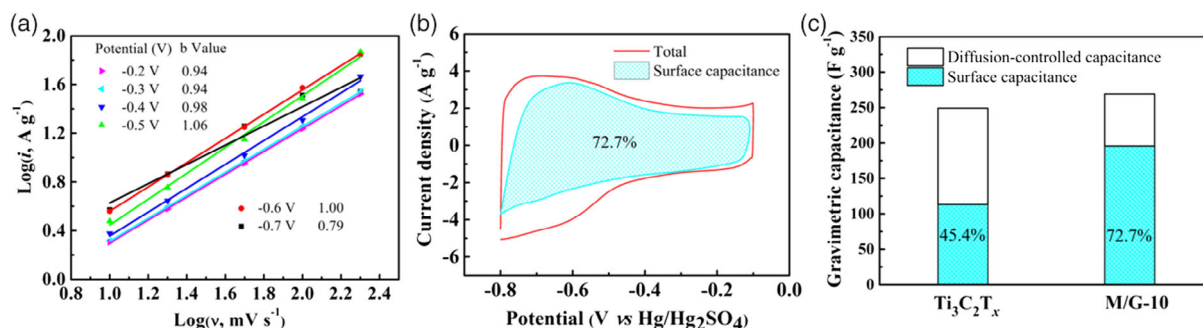


Figure 5. a) The relationship between current and scan rates from 10 to 200 mV s^{-1} for the M/G-10 electrode under different voltages. b) CV curves of the proportion of the M/G-10 electrode surface capacitance to total capacitance at 10 mV s^{-1} . c) Surface-controlled capacitive and diffusion-controlled capacitance contribution of the $\text{Ti}_3\text{C}_2\text{T}_x$ and M/G-10 electrodes at 10 mV s^{-1} .

the main factor affecting specific capacitance. However, we can clearly see from Figure S9, Supporting Information, that the specific surface area of M/G-10 is much larger than that of pure $\text{Ti}_3\text{C}_2\text{T}_x$. According to the energy-storage mechanism, the surface capacitance of the hybrid film is significantly higher than pure $\text{Ti}_3\text{C}_2\text{T}_x$. Therefore, it is reasonable to believe that the specific surface area is the more important parameter in determining the specific capacitance value among the synergies of various factors.

To understand the impact of the load of the electrochemically active material per unit area on the capacitance, we compared the capacitance of the composite film loadings from 1.80 to 3.08 and 4.17 mg cm^{-2} , respectively, and the areal specific capacitance correspondingly increases from 428.6 to 657.1 and 828.6 mF cm^{-2} (Figure S12a, Supporting Information). However, the gravimetric specific capacitance is gradual decreasing, and the capacitance drops from 240.1 to 215 and 198 F g^{-1} (Figure S12b, Supporting Information). Figure S12c, Supporting Information, shows that the relaxation time constant increases τ_0 from 1.47 to 5.56 s as the per unit area load increases from 1.80 to 3.08 mg cm^{-2} , indicating the increase in equivalent series resistance (internal resistance and charge transfer resistance) and decrease in ion transportation kinetics, resulting in the decrease in rate performance. In addition, compared with the 3.08 and 4.17 mg cm^{-2} electrodes, $C'(\omega)$ of the 1.8 mg cm^{-2} electrode decreases more slowly with the increase in frequency, which also indicates that the 1.80 mg cm^{-2} electrode has a smaller equivalent series resistance and excellent kinetics (Figure S12d, Supporting Information).

Symmetric supercapacitors were assembled and tested in 3 M H_2SO_4 aqueous electrolyte to evaluate the practical application performance of the composite electrode. Figure 6a shows the CV curves of M/G-10 electrode base symmetrical supercapacitor at different scan rates. It can be observed that the CV curves have no pronounced redox peaks and resemble those of carbon-based double-layer capacitors. Moreover, there is no noticeable distortion in the curves as the scan rates range from 2 to 200 mV s^{-1} , indicating excellent rate performance. The CV curves of a $\text{Ti}_3\text{C}_2\text{T}_x$ -based symmetrical supercapacitor are shown in Figure S13, Supporting Information. Figure 6b shows the gravimetric specific capacitance of $\text{Ti}_3\text{C}_2\text{T}_x$ and M/G-10-based symmetric supercapacitors at different scan rates, in which M/G-10 (94.5 F g^{-1}) is obviously larger than the specific capacitance of pure $\text{Ti}_3\text{C}_2\text{T}_x$ (70 F g^{-1}) at 2 mV s^{-1} . Figure 6c shows the Ragone plot of the symmetric supercapacitors. M/G-10-based symmetric supercapacitor with maximum gravimetric energy density of 13.1 Wh kg^{-1} can be achieved at a power density of 75 W kg^{-1} . Furthermore, an energy density of 5.28 Wh kg^{-1} increased to 3 kW kg^{-1} . It is clearly superior to $\text{Ti}_3\text{C}_2\text{T}_x/\text{RGO}$ -based symmetric supercapacitors of the same type previously reported, such as, $\text{Ti}_3\text{C}_2\text{T}_x/\text{RGO}$ film (10.5 Wh kg^{-1}),^[23] $\text{Ti}_3\text{C}_2\text{T}_x/\text{holey RGO}$ film (11.5 Wh kg^{-1}),^[22] and $\text{Ti}_3\text{C}_2\text{T}_x/\text{RGO}$ film (7.5 Wh kg^{-1}).^[21] The M/G-10-based symmetric supercapacitor exhibits excellent cyclic stability with retention of $\approx 110\%$ after 10 000 cycles at a current density of 5 A g^{-1} and coulombic efficiency that remains near 100% (Figure 6d). Meanwhile, pure $\text{Ti}_3\text{C}_2\text{T}_x$ -based symmetric supercapacitors also exhibit

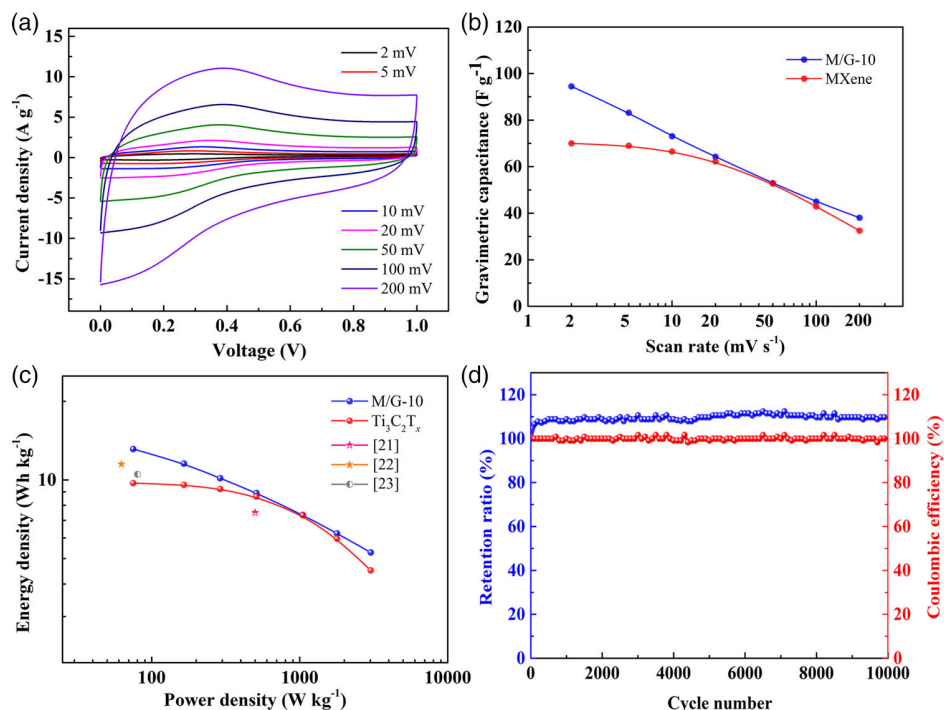


Figure 6. a) CV curves of M/G-10-based symmetric supercapacitor at different scan rates. b) Gravimetric specific capacitance of $\text{Ti}_3\text{C}_2\text{T}_x$ and M/G-10-based symmetric supercapacitor at different scan rates. c) Ragone plots of the gravimetric energy and power densities for $\text{Ti}_3\text{C}_2\text{T}_x$ and M/G-10-based symmetric supercapacitor. d) Cycling stability and coulombic efficiency of the M/G-10-based symmetric supercapacitor measured at 5 A g^{-1} for 10 000 cycles.

outstanding cyclic stability and coulombic efficiency (Figure S14, Supporting Information).

3. Conclusion

In summary, a facile strategy has been developed to prepare flexible self-supporting $\text{Ti}_3\text{C}_2\text{T}_x/\text{graphene}$ composite films through the use of large-sized-flakes $\text{Ti}_3\text{C}_2\text{T}_x$ and graphene nanosheets. The resulting composite film is not layer by layer self-assembled at the nanoscale by two different kinds of nanosheets, but graphene is introduced into the $\text{Ti}_3\text{C}_2\text{T}_x$ substrate in the form of free dispersion to reduce the self-stacking phenomenon of $\text{Ti}_3\text{C}_2\text{T}_x$, which can effectively improve ion diffusion dynamics and reduce charge transfer resistance. Specifically, it is mainly due to the increase in specific surface area rather than the interlayer spacing. This $\text{Ti}_3\text{C}_2\text{T}_x/\text{graphene}$ -10 composite electrode can not only achieve a high gravimetric specific capacitance of 269.2 F g^{-1} at a scan rate of 10 mV s^{-1} but also demonstrates a better rate capability with 207.3 F g^{-1} at a scan rate of 200 mV s^{-1} . The assembled self-supporting binder-free symmetric supercapacitor shows an ultrahigh gravimetric energy density of 13.1 Wh kg^{-1} at a power density of 75 W kg^{-1} and excellent cyclic stability after 10 000 cycles. This work provides new perspectives for the mechanism analysis of inhibiting self-stacking of MXene.

4. Experimental Section

Fabrication of Graphene Nanosheets: Graphene was obtained based on a modified version of the previously reported method.¹⁴⁰ The mass ratio of anhydrous ferric chloride (FeCl_3) to natural graphite flakes was controlled at 5:1. The mixture was placed in a stainless steel hydrothermal reactor (FQ-100-316L, Anhui Kemi Machinery Technology Co., Ltd.) and heated to 330° for 20 h; the product was then soaked in dilute hydrochloric acid (HCl) and ultrasonicated for 30 min, followed by water washing until it was clear and nearly colorless. After that, when NaBH_4 aqueous solution (2 wt%) was added, rapid volume expansion was observed, followed by vigorous stirring for 30 min to ensure adequate reaction of expansion stripping. The filtered products were added to 1 M HCl and stirred continuously for 24 h. Subsequently, the product was washed several times with ethanol and water, respectively. Finally, graphene nanosheets were obtained by freeze drying.

Synthesis of $\text{Ti}_3\text{C}_2\text{T}_x$ Aqueous Solution: $\text{Ti}_3\text{C}_2\text{T}_x$ was obtained by etching Ti_3AlC_2 powders with 12 M LiF/9 M HCl according to the modified version of the previously reported method.¹⁶ First, 0.8 g of lithium fluoride (LiF) was dissolved in 10 mL of 9 M HCl solution. Then, 0.5 g of Ti_3AlC_2 powder was slowly added into the above solution. The obtained mixture was maintained at 35°C for 24 h under stirring, after which the solid residue was washed with 1 M HCl, 1 M LiCl, and deionized water, respectively, until the pH value of the supernatant approached ≈ 6 . The precipitation was centrifuged repeatedly for 5 min (3500/rpm) to collect the upper $\text{Ti}_3\text{C}_2\text{T}_x$ aqueous solution. The concentration of the delaminated $\text{Ti}_3\text{C}_2\text{T}_x$ was determined by filtering a known volume of the $\text{Ti}_3\text{C}_2\text{T}_x$ aqueous suspension.

Fabrication of Flexible $\text{Ti}_3\text{C}_2\text{T}_x/\text{Graphene}$ Composite Films: The ethanol suspension of graphene (0.5 mg mL^{-1}) was added into 20 mL of $\text{Ti}_3\text{C}_2\text{T}_x$ suspension (1 mg mL^{-1}) drop by drop under stirring. The mixed solution was stirred for 10 min, followed by ultrasound for 10 min, and filtered using a mixed cellulose ester (MCE) membrane. Finally, the $\text{Ti}_3\text{C}_2\text{T}_x/\text{graphene}$ films were dried in a vacuum oven at 60°C for 12 h (denoted as M/G-x, where x is the mass ratio of graphene to $\text{Ti}_3\text{C}_2\text{T}_x$). M/G-5, M/G-10, and M/G-15 were obtained by changing the volume of graphene suspension with 2, 4, and 6 mL, respectively. For comparison, pure $\text{Ti}_3\text{C}_2\text{T}_x$ film was prepared without the presence of graphene.

Characterization and Electrochemical Measurements: Field-emission scanning electron microscopy (FESEM) of $\text{Ti}_3\text{C}_2\text{T}_x/\text{graphene}$ and $\text{Ti}_3\text{C}_2\text{T}_x$ films was conducted on a Hitachi S-4800, equipped with an EDS instrument (Hiroba). Field-emission transmission electron microscopy (FETEM) of MXene flakes was conducted on a JEM-2100F using an accelerating voltage of 200 kV. XRD patterns of the samples were obtained using a Rigaku D/max-2200pc diffractometer with $\text{Cu K}\alpha$ radiation ($\lambda = 0.15406 \text{ nm}$). The XPS was tested on a Thermo Fisher ESCALAB 250 spectrometer with an exciting source of Al $\text{K}\alpha$. Particle size distribution was measured using a laser particle size analyzer (Winner 2000). The Brunauer–Emmett–Teller (BET) tests were conducted on a model ASAP 2020 Plus Hd88 analyzer.

The electrochemical performances of the electrode materials were measured in a three-electrode Teflon Swagelok configuration, in which the prepared $\text{Ti}_3\text{C}_2\text{T}_x$ and $\text{Ti}_3\text{C}_2\text{T}_x/\text{graphene}$ flexible films, platinum disk, and $\text{Hg}/\text{Hg}_2\text{SO}_4$ in 3 M H_2SO_4 solution were used as the working, counter, and reference electrodes, respectively. The symmetric supercapacitors were assembled with two flexible films with the precisely same size separated by a glass microfiber membrane ($\Phi 6 \text{ mm}$, 1823-047 GF/D, Whatman, UK), which was used as the separator. All the electrochemical tests were conducted on a CHI 660E electrochemical workstation (CH Instruments, China) at ambient temperature. The cyclic voltammetry (CV) and GCD performances were tested, and the EIS was conducted at a frequency range from 0.01 Hz to 100 kHz with 5 mV of voltage amplitude at the open-circuit potential. The galvanostatic cycling stability was conducted on a LAND CT2001A instrument (Wuhan, China).

Supporting Information

Supporting Information is available from the Wiley Online Library or from the author.

Acknowledgements

This study was supported by the National Key Research and Development Program of China (grant 2017YFB0406301), the National Natural Science Foundation of China (52072295), the Fundamental Research Funds for the Central University, the 111 Project of China (B14040) and the “Young Talent Support Plan” of Xi’an Jiaotong University. The SEM and TEM works were done at the International Center for Dielectric Research (ICDR), Xi’an Jiaotong University, Xi’an, China, and the authors thank Ms. Yanzhu Dai and Mr. Chuansheng Ma for their help in using SEM and TEM.

Conflict of Interest

The authors declare no conflict of interest.

Data Availability Statement

Research data are not shared.

Keywords

electrochemical properties, graphene films, self-supporting, supercapacitors, $\text{Ti}_3\text{C}_2\text{T}_x$

Received: January 31, 2021

Revised: April 7, 2021

Published online:

- [1] Y. Gogotsi, B. Anasori, *ACS Nano* **2019**, *13*, 8491.
- [2] Y. Li, H. Shao, Z. Lin, J. Lu, L. Liu, B. Duployer, P. O. Å. Persson, P. Eklund, L. Hultman, M. Li, K. Chen, X. H. Zha, S. Du, P. Rozier, Z. Chai, E. Raymundo-Piñero, P. L. Taberna, P. Simon, Q. Huang, *Nat. Mater.* **2020**, *19*, 894.
- [3] M. Q. Zhao, X. Xie, C. E. Ren, T. Makaryan, B. Anasori, G. Wang, Y. Gogotsi, *Adv. Mater.* **2017**, *29*, 1702410.
- [4] G. Mu, D. Mu, B. Wu, C. Ma, J. Bi, L. Zhang, H. Yang, F. Wu, *Small* **2020**, *16*, 1905430.
- [5] D. Er, J. Li, M. Naguib, Y. Gogotsi, V. B. Shenoy, *ACS Appl. Mater. Interfaces* **2014**, *6*, 11173.
- [6] M. Alhabeab, K. Maleski, B. Anasori, P. Lelyukh, L. Clark, S. Sin, Y. Gogotsi, *Chem. Mater.* **2017**, *29*, 7633.
- [7] Z. Lin, H. Shao, K. Xu, P. L. Taberna, P. Simon, *Trends Chem.* **2020**, *2*, 654.
- [8] M. Ghidui, M. R. Lukatskaya, M. Q. Zhao, Y. Gogotsi, M. W. Barsoum, *Nature* **2014**, *516*, 78.
- [9] T. F. Li, X. D. Yan, L. J. Huang, J. H. Li, L. L. Yao, Q. Y. Zhu, W. Q. Wang, W. Abbas, R. Naz, J. J. Gu, Q. L. Liu, W. Zhang, D. Zhang, *J. Mater. Chem. A* **2019**, *7*, 14462.
- [10] H. Lin, X. G. Wang, L. D. Yu, Y. Chen, J. L. Shi, *Nano Lett.* **2017**, *17*, 384.
- [11] F. Shahzad, M. Alhabeab, C. B. Hatter, B. Anasori, S. M. Hong, C. M. Koo, Y. Gogotsi, *Science* **2016**, *353*, 1137.
- [12] A. Lipatov, M. Alhabeab, M. R. Lukatskaya, A. Boson, Y. Gogotsi, A. Sinitiskii, *Adv. Electron. Mater.* **2016**, *2*, 1600255.
- [13] C. J. Zhang, L. McKeon, M. P. Kremer, S. H. Park, O. Ronan, A. Seral-Ascaso, S. Barwich, C. O. Coileain, N. McEvoy, H. C. Nerl, B. Anasori, J. N. Coleman, Y. Gogotsi, V. Nicolosi, *Nat. Commun.* **2019**, *10*, 1795.
- [14] C. J. Zhang, M. P. Kremer, A. Seral-Ascaso, S. H. Park, N. McEvoy, B. Anasori, Y. Gogotsi, V. Nicolosi, *Adv. Funct. Mater.* **2018**, *28*, 1705506.
- [15] S. Abdolhosseinzadeh, R. Schneider, A. Verma, J. Heier, F. Nuesch, C. J. Zhang, *Adv. Mater.* **2020**, *32*, e2000716.
- [16] M. Yao, Y. Chen, Z. Wang, C. Shao, J. Dong, Q. Zhang, L. Zhang, X. Zhao, *Chem. Eng. J.* **2020**, *395*, 124057.
- [17] L. Li, N. Zhang, M. Y. Zhang, L. Wu, X. T. Zhang, Z. G. Zhang, *ACS Sustain. Chem. Eng.* **2018**, *6*, 7442.
- [18] L. Li, N. Zhang, M. Y. Zhang, X. T. Zhang, Z. G. Zhang, *Dalton Trans.* **2019**, *48*, 1747.
- [19] H. Chen, L. Y. Yu, Z. F. Lin, Q. Z. Zhu, P. Zhang, N. Qiao, B. Xu, *J. Mater. Sci.* **2020**, *55*, 1148.
- [20] Q. Yang, Z. Xu, B. Fang, T. Huang, S. Cai, H. Chen, Y. Liu, K. Gopalsamy, W. Gao, C. Gao, *J. Mater. Chem. A* **2017**, *5*, 22113.
- [21] B. Guo, J. Tian, X. Yin, G. Xi, W. Wang, X. Shi, W. Wu, *Colloids Surf., A* **2020**, *595*, 124683.
- [22] Z. M. Fan, Y. S. Wang, Z. M. Xie, D. L. Wang, Y. Yuan, H. J. Kang, B. L. Su, Z. J. Cheng, Y. Y. Liu, *Adv. Sci.* **2018**, *5*, 1800750.
- [23] J. Yan, C. E. Ren, K. Maleski, C. B. Hatter, B. Anasori, P. Urbankowski, A. Sarycheva, Y. Gogotsi, *Adv. Funct. Mater.* **2017**, *27*, 1701264.
- [24] C. Shen, L. Wang, A. Zhou, B. Wang, X. Wang, W. Lian, Q. Hu, G. Qin, X. Liu, *Nanomaterials* **2018**, *8*, 80.
- [25] W. Zhang, Z. Z. Pan, W. Lv, R. Lv, W. Shen, F. Kang, Q.-H. Yang, Y. Weng, Z. H. Huang, *Carbon* **2019**, *153*, 625.
- [26] K. Wang, B. Zheng, M. Mackinder, N. Baule, H. Qiao, H. Jin, T. Schuelke, Q. H. Fan, *Energy Storage Mater.* **2019**, *20*, 299.
- [27] J. L. Zheng, X. Pan, X. M. Huang, D. B. Xiong, Y. Shang, X. X. Li, N. Wang, W. M. Lau, H. Y. Yang, *Chem. Eng. J.* **2020**, *396*, 124057.
- [28] X. Wang, R. Wang, Z. Zhao, S. Bi, Z. Niu, *Energy Storage Mater.* **2019**, *23*, 269.
- [29] Y. A. Wang, Y. Wang, P. P. Zhang, F. Liu, S. D. Luo, *Small* **2018**, *14*, 1802350.
- [30] J. Halim, S. Kota, M. R. Lukatskaya, M. Naguib, M. Q. Zhao, E. J. Moon, J. Pitock, J. Nanda, S. J. May, Y. Gogotsi, M. W. Barsoum, *Adv. Funct. Mater.* **2016**, *26*, 3118.
- [31] W. Li, Z. Song, J. Zhong, J. Qian, Z. Tan, X. Wu, H. Chu, W. Nie, X. Ran, *J. Mater. Chem. C* **2019**, *7*, 10371.
- [32] Y. Tian, W. Que, Y. Luo, C. Yang, X. Yin, L. B. Kong, *J. Mater. Chem. A* **2019**, *7*, 5416.
- [33] M. R. Lukatskaya, S. M. Bak, X. Q. Yu, X. Q. Yang, M. W. Barsoum, Y. Gogotsi, *Adv. Energy Mater.* **2015**, *5*, 1500589.
- [34] H. Shao, K. Xu, Y. C. Wu, A. Iadecola, L. Liu, H. Ma, L. Qu, E. Raymundo-Piñero, J. Zhu, Z. Lin, P. L. Taberna, P. Simon, *ACS Energy Lett.* **2020**, *5*, 2873.
- [35] S. Fleischmann, J. B. Mitchell, R. Wang, C. Zhan, D. E. Jiang, V. Presser, V. Augustyn, *Chem. Rev.* **2020**, *120*, 6738.
- [36] C. Zhan, M. Naguib, M. Lukatskaya, P. R. C. Kent, Y. Gogotsi, D. E. Jiang, *J. Phys. Chem. Lett.* **2018**, *9*, 1223.
- [37] H. Lindstrom, S. Sodergren, A. Solbrand, H. Rensmo, J. Hjelm, A. Hagfeldt, S. E. Lindquist, *J. Phys. Chem. B* **1997**, *101*, 77172.
- [38] H. Shao, Z. Lin, K. Xu, P. L. Taberna, P. Simon, *Energy Storage Mater.* **2019**, *18*, 456.
- [39] J. Wang, J. Polleux, J. Lim, B. Dunn, *J. Phys. Chem. C* **2007**, *111*, 14925.
- [40] X. Qiao, Z. Lin, Y. Y. Si, X. D. Lin, S. W. Cui, X. S. Hu, *Key Eng. Mater.* **2017**, *744*, 458.